Surface topography effects on pool boiling via non-equilibrium molecular dynamics simulations

Alessio D. Lavino,*,† Edward Smith,‡ Mirco Magnini,¶ and Omar K. Matar†

†*Department of Chemical Engineering, Imperial College London, South Kensington Campus, London SW7 2AZ, UK*

‡*Department of Mechanical and Aerospace Engineering, Brunel University London, Uxbridge, Middlesex UB8 3PH, UK*

¶*Department of Mechanical, Materials and Manufacturing Engineering, University of Nottingham, NG7 2RD Nottingham, UK*

E-mail: alavino@ic.ac.uk

Abstract

In this work we investigate nucleate pool boiling via non-equilibrium molecular dynamics (NEMD) simulations. The effect of nano-structured surface topography on nucleation and transition to a film-like boiling regime is studied at the molecular scale, by varying the cavity aspect ratio, wall superheat, and wettability through a systematic parametric analysis conducted on a Lennard-Jones (LJ) system. The interplay of the aforementioned factors is rationalized by means of a classical nucleation theory-based model. The solid surface is heated uniformly from the bottom in order to induce the nanobubble nucleation. Insight into the cavity behavior in heat transfer problems is achieved by looking at temperature and heat flux profiles inside the cavity itself, as well as at the time of nucleation, for different operating conditions. The role of the cavity

size in controlling the vapor embryo formation is highlighted and its dependence upon the other investigated parameters summarized in a phase diagram. Our results show that heterogeneity at the nanoscale plays a key role in determining pool boiling heat transfer performance, suggesting a promising approach to optimize nano-structured surfaces for energy and thermal management applications.

Introduction

Pool boiling represents one of the most challenging and ubiquitous processes in thermal management systems. Its importance is due to its many applications[1,2] from nano/micro cooling devices in electronics[3] to macro-scale heat exchangers in the oil and gas industry[4]. This makes boiling systems a rapidly-growing area in the study of heat transfer, in which optimization at different length scales has been widely investigated in the last decade from both the modeling[5–7] and experimental[8–10] perspectives. Yet despite the considerable attention received by pool boiling in the literature, there remain a number of open problems. A complete understanding of the microscopic origins of boiling is lacking, together with a comprehensive picture of how the solid surface interacts with the fluid during the onset of nucleation. This partial understanding has limited the optimization of solid surfaces which are central to the manufacturing and design of heat transfer units.

Surface topography has been shown to play a key role in enhancing boiling heat transfer performances[11]. It is currently possible to produce nano-structured surfaces (e.g., nanowires) with tunable and desired specifications, leading to higher surface morphology control[12–14]. Due to the complexity of the phenomena involved, as well as the multiscale nature of pool boiling, different modeling approaches are required depending on the length scale under consideration. Meso-[15,16] and macro-scale[17,18] models provide insights into the departure diameter and frequency of the nucleated bubbles. Most of these approaches, however, use assumptions (e.g. local equilibrium or linear non-equilibrium) to reproduce the physics of phase change, especially in close proximity to the solid-liquid interface.

Pool boiling is a complex, spatially-inhomogenous, non-equilibrium process, dependent on the nature of the solid-liquid interactions that cannot be accounted for by existing meso- and macro-scale models. Molecular-scale investigations, therefore, appear to be a promising approach to pool boiling modeling, since the out-of-equilibrium nature of boiling, and the effects of molecular interactions, are captured at the atomistic scale[19], without the need for any closure assumptions. More specifically, surface wettability and geometrical details can be built into the model. The advantage of molecular modeling of pool boiling is twofold: first, it provides insights and useful information that can be passed to larger-scale models; second, key phenomena and fundamentals can be investigated by looking at the atomistic nature of phase change.

Molecular dynamics (MD)[20] has been widely employed in the last few years to provide molecular-scale insights into the complexity of boiling phase change at the nano/micro-scale[19,21–23]. Previous attempts at the MD level investigated extensively the role of wettability on heat transfer performances for Lennard-Jones (LJ) liquid argon systems. Tang *et al.*[24] studied the effect of bare and graphene-coated surfaces for atomically smooth solid wall systems and their influence on critical heat flux (CHF) and transition to film (explosive) boiling for liquid LJ argon. A local, non-uniform heating spot was investigated by Yamamoto and Matsumoto[25] with particular attention to wettability heterogeneities on smooth (flat) solid walls. They confirmed that no pre-existing nuclei are needed to induce the onset of nanobubble nucleation at the molecular scale. The authors proved that wettability affects boiling inception, due to the wall-liquid energy interaction. Diaz *et al.*[26,27] investigated the effect of wettability on nano-patterned surfaces. The authors mainly focused on the effect of solid-fluid interactions on CHF. Yin *et al.*[28,29] investigated the effect of nanoparticles in a cavity showing an increase of heating performances. Novak *et al.*[30] showed that high aspect ratio indentations lead to a better control of nucleation rate than lower ones. The authors stated that wall defects size can improve the control of the nanobubble nucleation. The importance of the presence of cavities in the solid wall was also confirmed by Chen

et al.[31,32] who studied the thermal performances of rough surface and their benefits with respect to the smooth ones. These investigations showed that the enhancement of thermal properties brought about by the surface roughness is also related to solid-liquid interactions. Other works on cavity effects have also been recently conducted[33,34], stressing even further the importance of a surface post/defect in nucleate boiling. More specifically, Mukherjee et al.[34] studied water bubble growth rate as a function of the notch geometry; the more recent work of Shahmardi et al.[33] highlighted the importance of a surface defect (square cavities) in triggering the nanobubble nucleation, mainly focusing on the energy fields at constant cavity size. Further investigations have also been made by Zhou et al.[35] who conducted an interesting analysis on the non-trivial role played by the surface wettability in relation to different wall superheat, in terms of nucleation time for flat surfaces. The importance of the wettability role is also confirmed by Chen et al.[36], Hens et al.[37] and Shavik et al.[38] who mainly investigated explosive boiling regimes for LJ liquid argon systems, at very high wall temperatures (above 200 K), on flat solid surfaces.

Despite the extensive investigations reported above, a lack of knowledge on the defects/cavities role in nanobubble nucleation is still present, and the interplay among surface topography, wall heating, and wettability remains partially-understood which limits our ability to control pool boiling. More importantly, an open and fundamental question still concerns the role played by the cavity size and how this is related to the other operating parameters. Hence, our novel contribution goes into the direction of highlighting the role played by the cavity size in driving and control nanobubble formation, through a systematic parametric analysis. Additionally, we aim at proposing a mathematical modeling approach which can rationalize our MD observations and, at the same time, constitute a solid bridge with a more general multiscale approach.

In this paper, non-equilibrium molecular dynamics (NEMD) is used to investigate the surface topography effect on nucleate pool boiling for a Lennard-Jones (LJ) system. The main advantage of investigating a LJ system is brought by the low computational cost at

which a wide range of operating conditions (physical and chemical, e.g., wettability) can be easily investigated without any loss of generality. On the other hand, electrostatic interactions and the complexity of molecules geometry cannot be taken into account in this simplified approach. This leads to another advantage which consists in the possibility of investigating single factors at the time, to study such a complex process like pool boiling. The main novelty of this work is the performance of a systematic study of the role played by the cavity size in the solid wall on nanobubbles nucleation, together with the effect of the surface wettability and wall superheat. The interplay among these factors is studied extensively and summarized in a phase diagram, in terms of nucleation time, cavity behavior, and key mechanisms observed. This represents a crucial step forward in the study and the understanding of the ability of a solid surface defect/post (i.e., cavity) to provide more or less control on the nucleated vapor embryo. We also show how nucleation data from MD can be interpreted by a classical nucleation theory (CNT)-based model. As a further element of novelty, the CNT-based model represents a powerful tool not only to describe the nucleation time but also to rationalize the interplay of the aforementioned factors. Furthermore, the cavity heat transfer performance is evaluated quantitatively in terms of heat flux and temperature inside the cavity and compared to the predictions of a continuum-scale, one-dimensional heat diffusion model to further understand the main mechanisms involved at such short time- and length-scales. These modelling investigations are of paramount importance for a future link to upper-scale models in a more general multiscale framework. Our results can be applied to the design of surface topography to control nanobubble nucleation for optimal heat transfer performance and thermal management of nano-devices.

The rest of this paper is structured as follows: we first show the numerical details and operating conditions of the investigated system; main results and general discussion are then reported. Conclusions and future perspectives are provided in the final part of the manuscript. Details of the relationship between Lennard-Jones reduced units and SI real units are summarized in supporting information.

Molecular dynamics: computational setup & operating conditions

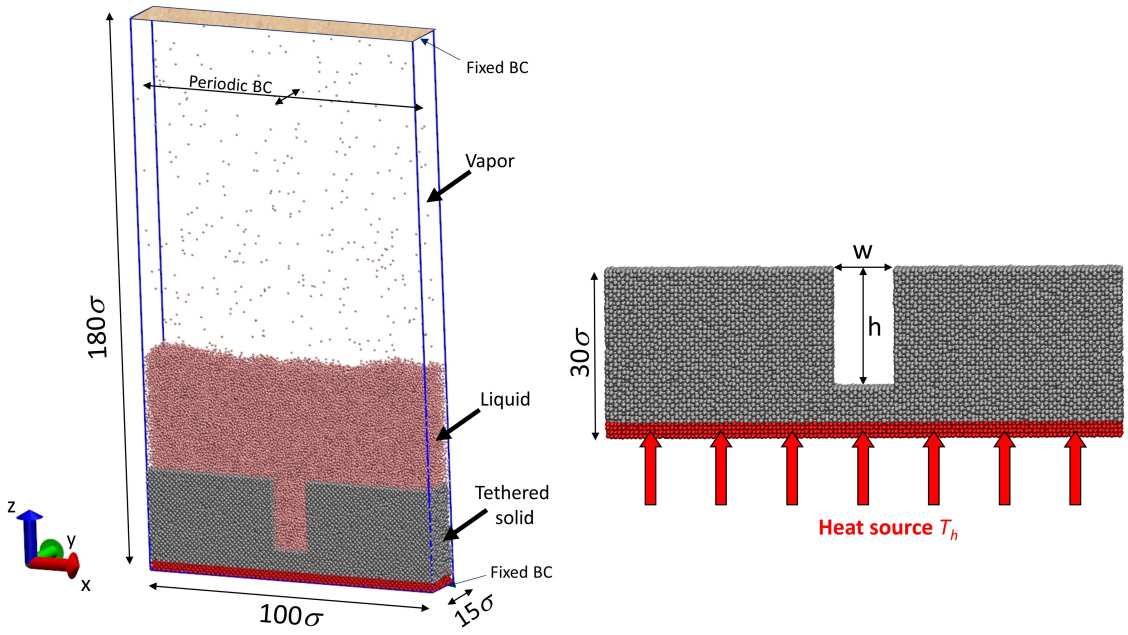

Figure 1: Schematic representation of the simulation box, left, and geometry of the solid wall, right, with cavity size of width w and depth $h = 20\sigma$ (constant). The aspect ratio is defined as $AR = w/h$. The solid surface is uniformly heated from the bottom (red) with temperature T_h.

A schematic representation of the simulated system is shown in Figure 1. It consists of 10^5 Lennard-Jones (LJ) particles which interact through a pairwise Lennard-Jones (LJ) potential:

$$\phi(r_{ij}) = \begin{cases} 4\varepsilon_{ij}\left[\left(\frac{\sigma_{ij}}{r_{ij}}\right)^{12} - \left(\frac{\sigma_{ij}}{r_{ij}}\right)^{6}\right] & r_{ij} \leq r_{out} \\ 0 & r_{ij} > r_{out} \end{cases}, \tag{1}$$

where ε_{ij} and σ_{ij} are the energy and the distance parameters between two generic atoms i and j, at distance r_{ij}. The higher the value of ε_{ij}, the more energetically intense is the interaction between atoms i and j; no electrostatic effects are taken into consideration. An outer cutoff radius $r_{out} = 2.9\sigma$ is used and the potential function reported in Equation (1) is smoothly

varied to zero between a distance $r_{in} = 2.5\sigma$ and r_{out} using a fourth-order polynomial with coefficients C_1, C_2, C_3, C_4 chosen so force $F(r_{ij}) = C_1 + C_2(r - r_{in}) + C_3(r - r_{in})^2 + C_4(r - r_{in})^3$ varies smoothly to zero. This smooth tail prevents the system undergoing singularities (due to cutoff noise) during the MD time integration[39]. Furthermore, reduced LJ units are used throughout this work, with the aim to study general fluid dynamics in a simple system. The correspondence with real SI units is summarized in supporting information.

As shown in Figure 1, in reduced units the simulation box size is $100\sigma \times 15\sigma \times 180\sigma$, respectively in x, y, and z; therefore, a pseudo two-dimensional approach is adopted with the advantage of capturing the main physics of boiling at a low computational cost, despite maintaining a wide system in x and z (vertical) directions. The solid surface is placed at the bottom (gray and red) and is generated in the face-centered cubic (FCC) lattice with a reduced density equal to 1. Liquid and vapour phase atoms are placed with a number density equal to 0.69 and 0.01, respectively. Solid atoms are tethered to their equilibrium positions by a harmonic spring force with a spring constant equal to 100. This avoids translational movements and penetration by liquid phase atoms during the simulation run.

The top and bottom faces of the simulation box (perpendicular to z-direction) are characterized by fixed boundary conditions (12/6 LJ interactive wall on top and fixing a one-way velocity sign for the particles on bottom side), while periodic boundary conditions are imposed in the x- and y-directions. The right side of Figure 1 depicts the structural detail on the solid wall: a cavity of width w and depth h is placed in the center. The size of the cavity is characterized throughout the whole work in terms of its aspect ratio, AR:

$$AR = \frac{w}{h}, \tag{2}$$

where the cavity depth h is constant and w is varied parametrically in order to investigate the range $AR = 0.25 - 2.0$. Solid-solid, s, and fluid-fluid, f, interactions are governed by the following LJ parameters: $(\varepsilon_{ss}, \sigma_{ss}) = (3.08, 0.85)$, and $(\varepsilon_{ff}, \sigma_{ff}) = (1.0, 1.0)$. The

cross interactions between solid and fluid atoms, ε_{sf}, determines surface wettability[40] and will be explicitly set to suitable values that can guarantee the desired hydrophilicity degree. Consequently, based on their values, three different scenarios are possible:

$$\frac{\varepsilon_{sf}}{\varepsilon_{ff}} \rightarrow \begin{cases} < 1 & \text{hydrophobic,} \\ = 1 & \text{neutral,} \\ > 1 & \text{hydrophilic.} \end{cases}$$

In this work, hydrophobic, neutral, and hydrophilic surfaces are studied and the corresponding solid-liquid LJ parameters are $(\frac{\varepsilon_{sf}}{\varepsilon_{ff}}, \frac{\sigma_{sf}}{\sigma_{ff}}) = (0.5, 1.05)$, $(1.0, 1.00)$ and $(1.7, 0.93)$, respectively .

The initial configuration of the system is minimized by applying a conjugate gradient (CG) algorithm with a stopping tolerance for both energy (unitless) and force (force units) equal to 10^{-8}. The system is then equilibrated in a constant molecular number (N), constant volume (V) and constant temperature (T) ensemble (NVT), using a Nose-Hoover thermostat[41] with characteristic relaxation time constant equal to $100\Delta t$, where Δt is the value of the time-step set equal to 0.005τ, in which τ represents the characteristic time in reduced LJ units (see supporting information). NVT equilibration is run for 50000 time-steps which brings the system to the target temperature $T_{cold} = 0.8$; temperature values are provided in reduced LJ units (see supporting information) throughout this work. After equilibration, simulations are run in NVE ensembles for $3\times10^6\Delta t$ with a timestep $\Delta t = 0.005\tau$. The equations of motion for the atoms are time-integrated using the standard velocity-Verlet integrator algorithm.

Heat is provided uniformly from the bottom (represented in red in Figure 1) by thermostatting the solid substrate with a thickness of 3σ to $T_h = [1.2 - 2.2]$, using the Langevin

thermostat[42]. We investigate the effect of the wall superheat, ΔT_{wall}, defined as

$$\Delta T_{wall} = T_{wall} - T_{sat}, \tag{3}$$

which represents the difference between the wall temperature T_{wall} and the liquid saturation temperature, T_{sat}, that corresponds to about 1.01 at the investigated operating conditions and in line with other works performed on LJ systems[23]. As common practice,[23,24] T_{sat} is determined by NVT simulations at increasing fluid temperatures T. T_{sat} corresponds to the minimum temperature beyond which a nucleus appears within the limit of the simulation time. We are aware that the saturated temperature will change in a non-trivial manner as the system is heated, at different points of the fluid. However, the only use of T_{sat} is in defining the relative superheat ΔT_{wall}, and therefore using a constant value for all cases presented can be considered a good approximation for the purposes of the current work. In this work, T_{wall} is considered to be the spatially-averaged wall temperature of the gray solid surface depicted in Figure 1, which varies over time, due to the non-equilibrium nature of the performed MD analysis. The range of wall superheats studied here is $\Delta T_{wall} = [0.2 - 1.2]$.

In line with its definition[43], the heat flux vector is evaluated from MD trajectories as:

$$\mathbf{J} = \frac{1}{V}\left[\sum_i (e_i \mathbf{v}_i) + \frac{1}{2}\sum_{i<j} \left(\mathbf{F}_{ij} \cdot (\mathbf{v}_i + \mathbf{v}_j)\right) \mathbf{r}_{ij}\right], \tag{4}$$

where V is the volume of the region in which the heat flux is evaluated, e_i corresponds to the total energy (potential plus kinetic) of each atom i, $\mathbf{v}_i$ is the per-atom velocity vector. The second term inside the square brackets corresponds to the virial contribution of the per-atom stress tensor, where $\mathbf{F}_{ij}$ is the force acting on atom i due to the pairwise interaction with an atom j, at distance $\mathbf{r}_{ij}$. MD simulations are carried out by means of the Large-scale Atomic/Molecular Massively Parallel Simulator (LAMMPS) package[44]. The VMD software[45] is used to produce graphical images of the molecular systems.

Results and discussion

Below, we present the results starting with a preliminary analysis of the nucleation event. Then, nucleation boiling is extensively investigated and transition to film-like boiling is presented in the third part of this section. Heat transfer results are then shown and, finally, the main findings of this MD parametric study are summarized in a phase diagram.

Preliminary observation of nucleation events

We begin the presentation of our results by showing a nucleation event for flat hydrophobic and hydrophilic surfaces in Figure 2, characterized by $AR = 0$. The wall superheat is $\Delta T_{wall} = 0.2$, as previously defined in Equation (3). Inspection of Figure 2 reveals that nucleation takes place differently, depending on the surface wettability, in line with previous investigations[26]. As can be seen in Figure 2(a), the nanobubble is in direct contact with the hydrophobic solid surface, whereas in the case of the hydrophilic surface shown in Figure 2(b), a thin liquid layer is formed between the nuclei and the solid wall. As will be shown later, film-formation has a direct bearing on the heat transfer performance of the solid wall for the full range of cases investigated.

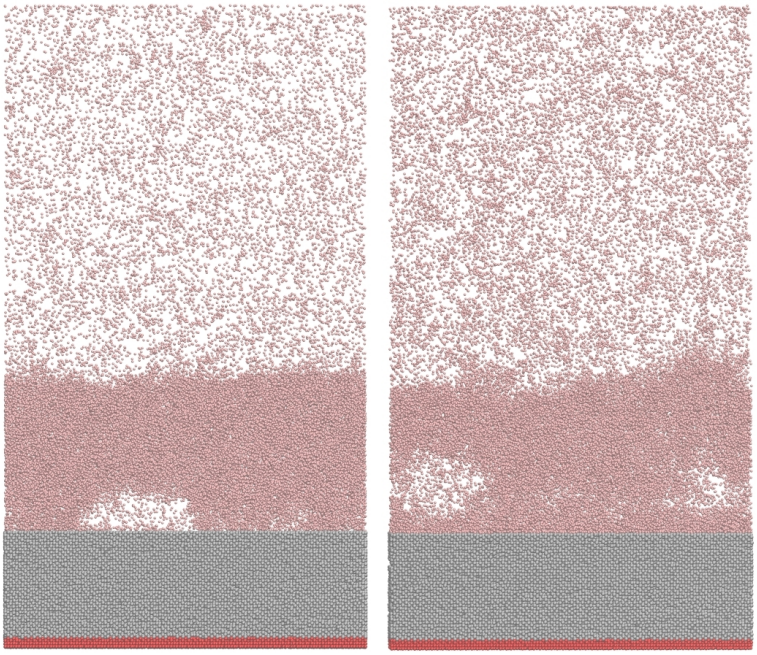

(a) (b)

Figure 2: Nucleation events for flat hydrophobic and hydrophilic surfaces, shown in (a) and (b), respectively, characterized by $AR = 0$, $\Delta T_{wall} = 0.2$, and the corresponding wettability parameters reported in the operating conditions section.

Importantly, the nucleus forms randomly in the bulk liquid proving that the flat surface provides very little control over the onset of nucleate boiling. Due to the stochasticity of the nucleation process and in the absence of surface-structuring, a nucleus appears spontaneously when the liquid has sufficient energy to expand locally. In contrast, and as will be shown below, in the case of nano-structured surfaces, the nucleation dynamics is characterized by a deep interplay between the cavity size, the wettability conditions, and the wall superheat.

Snapshots depicting the dynamic evolution (at 2500τ simulation time intervals) from nanobubble nucleation to continuous vapour film formation are presented in Figure 3 at cavity $AR = 0.50, 1.0$, and $\Delta T_{wall} = 0.2$ for the hydrophobic (top panel) and hydrophilic (bottom panel) surfaces. Similar results associated with the rest of the parameters and cases studied in this work (i.e., all the wettability and cavity AR ranges) can be found in the Supporting Information (SI). Every nucleation event takes place at a different time, depending on wettability and cavity aspect ratio, as will be shown in the Nucleation time subsection. It

is clear from Figure 3 that for the smallest AR values studied the cavity is filled with liquid in the case of hydrophilic and neutral surfaces (see SI), resulting in nucleation events that originate outside the cavity itself, either on the heated surface or within the liquid bulk.

For non-hydrophobic surfaces and very small cavity AR (i.e., $AR = 0.25$ and 0.50, see Figure 3(i)-3(l) and SI), formation of multiple nanobubbles is also possible which could merge resulting in faster development of continuous vapour films separating the solid and liquid phases. In these cases, the solid surface has very little influence on the onset of nanobubble nucleation dynamics. On the other hand, for the hydrophobic surface, nucleation occurs within the cavity at all AR studied and the resulting nanobubble remains localized in the vicinity of the vapour-filled cavity. This illustrates the fact that for hydrophobic surfaces, even narrow cavities can provide control over the location of the onset of nanobubble nucleation, despite the transition to a film-like boiling regime (i.e., vapour blanket covering the entire solid surface) occurring at much earlier simulation times. This is demonstrated by the snapshots depicted in Figure 3(a)-3(h) and will be discussed in detail in the following sections. It is worthwhile to stress that these results are achieved and therefore valid for a cavity post that is placed in a system of characteristic dimensions of few hundreds molecular units σ for the solid surface design. Moreover, we have performed additional larger scale MD simulations (simulation box 3 times bigger, $2.5 \cdot 10^6$ particles) and observed that some similarities can be reached, at least in terms of nucleation time and dynamics of nanobubble formation, despite the dynamics of the nanobubble growth is substantially different. This analysis is here omitted as out of the main scope of this work but paves the way for deeper future investigations; however, a demonstrative comparison is reported in Appendix A.

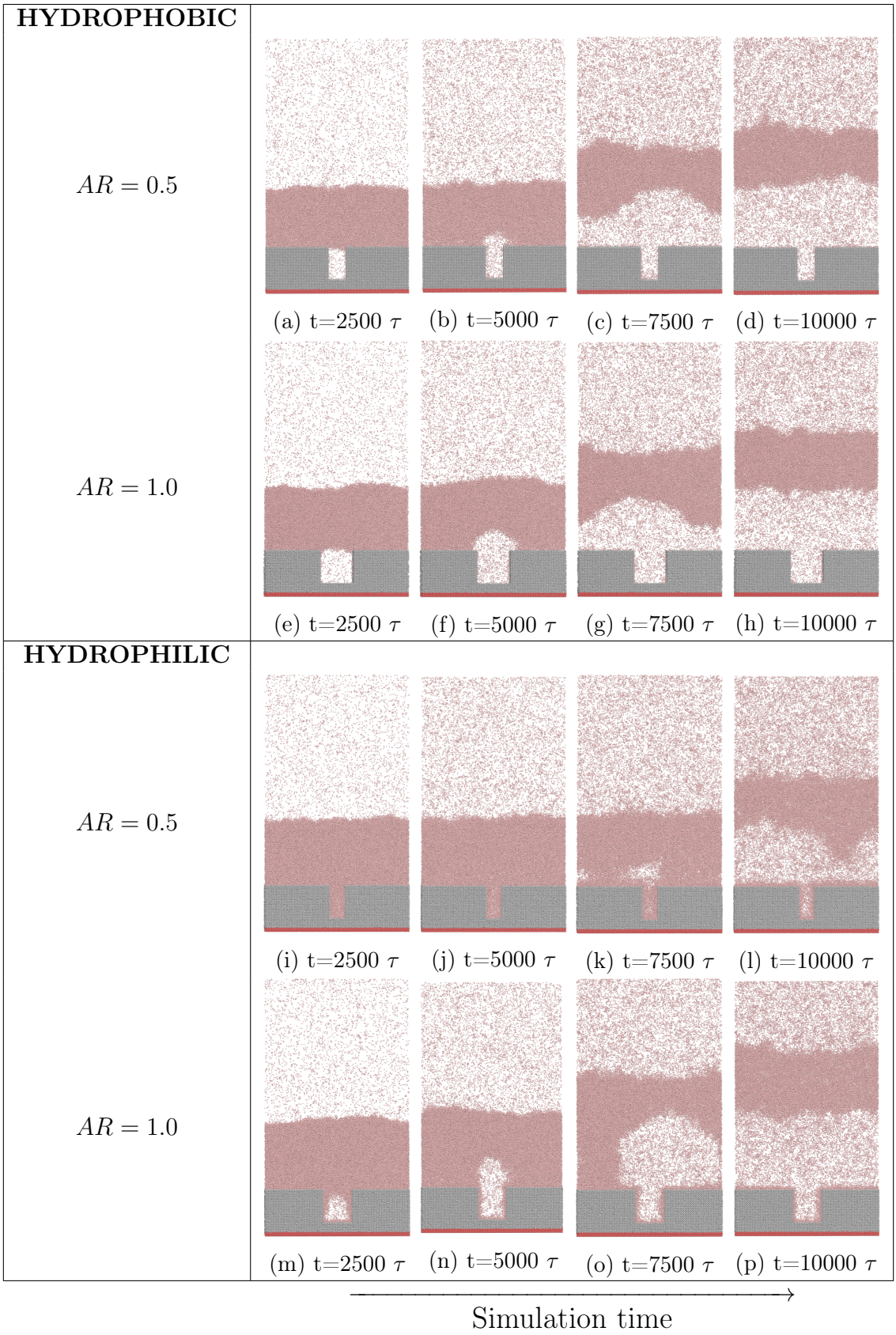

Figure 3: Evolution of nucleate boiling process at 2500τ simulation time intervals, at cavity aspect ratios $AR = 0.5, 1.0$, for the hydrophobic (a-h, top panel) and hydrophilic (i-p, bottom panel) surfaces at $\Delta T_{wall} = 0.2$.

The ability of the system to ensure that a vapour region is constantly replenished by an adjoining liquid phase (following bubble departure) is defined as 'capillary pumping' and represents one of the key properties of nano-structured surface design and manufacturing for heat transfer processes optimization[46]. As seen in Figure 3, although the wide cavity sizes (high AR) offer a higher degree of control over the nucleation site they hinder the constant presence of liquid phase in the cavity; the mass of liquid that collects in a cavity of given AR is also an increasing function of the surface wettability. This might constitute an unwanted effect for the capillary pumping during the boiling process. With increasing AR, the qualitative differences in system behavior associated with surface wettability are reduced, as demonstrated by Figure 3 (and for cavity $AR > 1$ in the SI); furthermore, the advantage of a more controllable nucleation site is counterbalanced by a faster transition to film-like boiling regime, which provides thermal resistance to heat transfer (see the Heat transfer analysis subsection).

Nucleation time

We now investigate the nucleation time t_{nucl}, expressed in reduced LJ units τ, as a function of the wall superheat, ΔT_{wall}, for different cavity aspect ratios AR, and constant wettability defined by the LJ potential parameters in the operating conditions section. This is reported in Figure 4 for the case of a hydrophilic surface. Within our MD framework, the presence of a nucleus is identified when a part of the liquid phase (density $\rho_{liq} \approx 0.7\sigma^{-3}$) expands and a vapor phase, an order of magnitude lower in density (as also visible in Figure 2, density $\rho_{vap} \approx 0.01\sigma^{-3}$), appears and stably persists for the remainder of the simulation for a minimum number of timesteps $n_{min} > 5 \cdot 10^3$. This can be assessed using cluster analysis on the molecules or computer vision on the density fields, but visual inspection is found to be sufficient for the number of cases study in this work. This can occur inside or outside the cavity, depending on the operating conditions, as seen in Figure 3 (and the SI). When nucleation happens outside the cavity, t_{nucl} is the elapsed time of the simulation till the

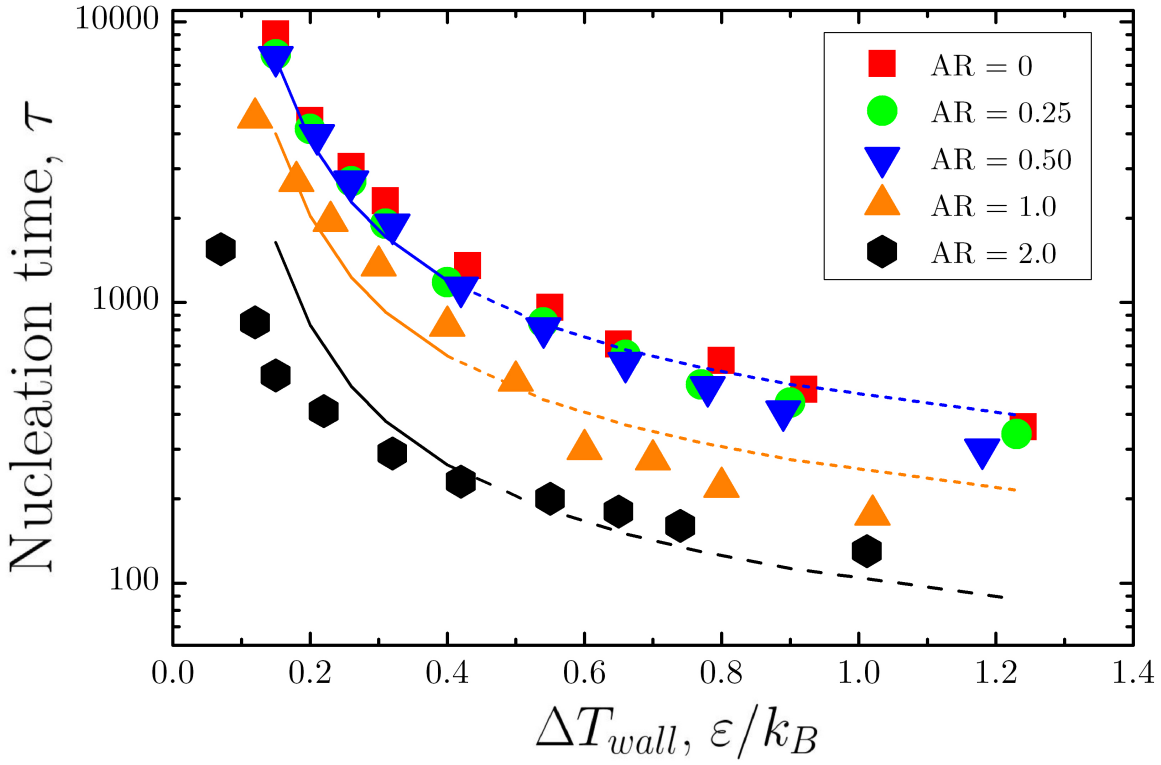

Figure 4: Variation of the nucleation time in reduced LJ units τ, with the wall superheat ΔT_{wall} for a hydrophilic surface of varying aspect ratio, AR, and wettability parameters defined in the operating conditions section. Simulation results are represented with discrete symbols, while the corresponding theoretical fitting (classical nucleation theory, Equation (9)) is reported with dashed lines.

bubble is created. When nucleation occurs inside the cavity, t_{nucl} is the elapsed time of the simulation till the bubble emerges from the cavity.

As can be seen in Figure 4, t_{nucl} decreases with increasing ΔT_{wall} and also decreases with increasing cavity width AR. The latter effect is due to the fact that with increasing AR, a larger surface area is closer to the heat source. For $\Delta T_{wall} > 0.5$, nucleation is heat transfer-dominated and weakly-dependent on AR (the graph is on a semi-logarithmic scale), with the nucleation time appearing to reach a plateau at large ΔT_{wall} values. For $\Delta T_{wall} < 0.5$, on the other hand, t_{nucl} increases rapidly with decreasing ΔT_{wall}, suggesting that small variations in wall superheat lead to large variations in time to nucleation event. Furthermore, for

$\Delta T_{wall} < 0.5$, t_{nucl} is weakly-dependent on AR in the range $AR \in [0 - 0.5]$. Under these operating conditions (hydrophilic wall) the nucleated embryo forms outside the liquid filled cavity. The cavity therefore acts to transfer heat only, with a negligible impact on the nucleation event. When $AR \geq 1$, t_{nucl} exhibits strong dependence on AR as exemplified by the $AR = 2$ case. The trends shown in Figure 4 lead to the conclusion that AR and ΔT_{wall} play a dominant role in time to nucleation when $\Delta T_{wall} < 0.5$ and $AR \geq 0.5$.

To quantify the importance of AR and ΔT_{wall}, we propose a classical nucleation theory (CNT)-based approach which is fitted to the MD results reported in Figure 4 (lines).[40,47,48] Continuous lines are used until $\Delta T_{wall} = 0.4$, dashed lines are employed afterwards to stress the concept that CNT may be not valid anymore after the fluid reaches supercritical conditions. For a liquid LJ system this might take place for liquid temperature values around 1.4. It is important to stress, however, that in the whole range of operating conditions adopted in this work and within the simulation time no supercritical behaviour was detected by the fluid phase. In line with CNT, the nucleation rate, J_N, can be generally expressed as:

$$J_N = CD_* Z \exp\left[-\frac{\Delta G^*}{k_B T}\right], \tag{5}$$

where k_B is the Boltzmann constant and T is the temperature in dimensional units; ΔG^* is the peak (nucleation energy barrier) of the free energy related to phase transition. The CD_* and Z terms account for the kinetics of phase transition and the related probability, respectively. The kinetics are expressed as a collision frequency and Z is the Zeldovich factor which corresponds to the probability that a nucleus at the top of the energy barrier will form the new phase, instead of dissolving into the liquid phase (due to density fluctuations around

the peak of ΔG profile). The factors C, D_*, and Z can be expressed as:[48]

$$\begin{aligned} C &= \hat{\rho}^2, \\ D_* &\sim \lambda(v_*) k_B T, \\ Z &= \left(\frac{4\gamma}{k_B T A_*^2} \right)^{1/2}, \end{aligned} \tag{6}$$

where $\hat{\rho}$ is the number density of particles relative to the metastable liquid, A_* is the collision area (e.g., surface of the nucleus) of the critical bubble, γ is the surface tension, D_* is the molecular diffusion coefficient, with the assumption that the process is driven by Brownian motion (assuming fluid inertia is negligible);[48] λ is a proportionality coefficient, which is directly proportional to the critical volume v_* of the nanobubble. Under conditions of negligible inertia, and adopting a Maxwellian velocity distribution of the particles involved in the phase transition, Baidakov and Bobrov[48] demonstrated that $\lambda = \frac{3v_*}{4\eta}$, for viscosity η. By substituting the set of relationships reported in Equation (6) into Equation (5), and neglecting the temperature dependence of surface tension and viscosity of the fluid, the following simple proportionality relationship holds:

$$J_N \propto \hat{\rho}^2 R_* (k_B T)^{1/2} \exp\left[-\frac{\Delta G^*}{k_B T} \right], \tag{7}$$

where R_* is the characteristic critical radius. The term $\hat{\rho}^2 R_*$ represents a physical quantity that can be considered proportional to the collision area available for phase transition, as this term represents the number of metastable liquid particles per unit volume. The more particles in this thermodynamic state and the larger R_*, the higher is the collision area, hence the higher the probability that if a particle interacts with the nanobubble nucleus, then, it joins the forming embryo. Note that the proportionality relationship represented by Equation (7) is in agreement with classical expressions for the nucleation rate[40].

We now establish a mapping between the parameters appearing in Equation (7) and those that govern the nucleation dynamics in our present MD study. We take the collision

area $\hat{\rho}^2 R_*$ to be proportional to the cavity area $2h + w = h(2 + AR)$ (with w and h defined in Figure 1). This assumes that the wider the surface area that is in direct contact with the heat source, the higher the probability of having collisions which lead to a phase transition. We also use $k_B T \propto \Delta T_{wall}$ (and note that T_{wall} is expressed in LJ units; see Table A.1 in Appendix A). Since the nucleation rate J_N is inversely proportional to the nucleation time t_{nucl} [25,30,49] , the following relationship holds:

$$J_N \approx \frac{1}{t_{nucl}} \propto (2 + AR)\Delta T_{wall}^{1/2} \exp\left[-\frac{f(\varepsilon_{sf})}{\Delta T_{wall}}\right], \tag{8}$$

where the nucleation energy barrier ΔG^* has been replaced by the function $f(\varepsilon_{sf})$, which may be viewed as the ratio of heterogeneous to homogeneous nucleation energies, $f = \Delta G^*_{het}/\Delta G^*_{homo}$ [40], and a smoothly-increasing function of the fluid-solid interaction energy, ε_{sf}, solely; thus, the energy needed to create a nucleus increases with ε_{sf} and, therefore, with f. In the present work, it is the effect of the relative change in ε_{sf} and, in turn, of f, on nucleation that is of relevance rather than its absolute value. Rearranging Equation (8), the nucleation time t_{nucl} becomes:

$$t_{nucl} = \frac{c}{(2 + AR)\Delta T_{wall}^{1/2} \exp\left[-\frac{f(\varepsilon_{sf})}{\Delta T_{wall}}\right]}, \tag{9}$$

where the proportionality constant c and $f(\varepsilon_{sf})$ are considered as fitting parameters of the function t_{nucl} against ΔT_{wall}, with the aspect ratio AR varying parameterically.

The relationship expressed by Equation (9) corresponds to the continuous-dashed lines depicted in Figure 4. It is important to emphasize that the CNT-based theoretical fitting was applied only in cases where the nucleated embryo appears inside the cavity. In the other cases where the nucleus forms outside the cavity, the parameter AR no longer directly affects the onset of nucleation and hence Equation (9) is only applicable in the range $AR \in [0.5 - 2.0]$ for hydrophilic and $AR \in [0.25 - 2.0]$ for hydrophobic surfaces, as demonstrated clearly in Figure 4. In the latter case, nucleation always occurs inside the cavity, as shown by

our snapshots reported in Figure 3. Cavity AR larger than 2 were not investigated in this analysis, as very large AR values tend to a flat surface behavior and all the advantages brought by the presence of a nucleation spot fade out. This is further confirmed for the case $AR = 4$, shown in the supporting information. Equation (9) is fitted to the MD simulations data for nucleation time against wall superheat temperature by varying c for the range of AR values and $f(\varepsilon_{sf})$ for different wettability conditions. The values of the fitting parameters are reported in the supporting information. More specifically, for all AR values $f(\varepsilon_{sf}) = 0.32$ (hydrophilic), $f''(\varepsilon_{sf}) = 0.31$ (neutral), $f'(\varepsilon_{sf}) = 0.28$ (hydrophobic). The proportionality constant $c = (900, 850, 550, 300)$, corresponding respectively to $AR = (0.25, 0.50, 1.0, 2.0)$.

We now exploit the explicit functional dependence of t_{nucl} on AR and ΔT_{wall} provided by Equation (9) to rationalize the trends observed in Figure 4. It is seen clearly from Equation (9) that for $\Delta T_{wall} \gg f$ (with $f \approx 0.3$ in our study, see supporting information), the exponential term approaches unity, and,

$$t_{nucl} \sim \frac{1}{(2 + AR)} \Delta T_{wall}^{-1/2}. \tag{10}$$

This asymptotic relation indicates that at large ΔT_{wall}, and for a given AR, $t_{nucl} \sim \Delta T_{wall}^{-1/2}$, suggesting that in this limit the nucleation time is collision-dominated and independent of surface wettability. In the same limit of large ΔT_{wall}, and for $AR \gg 1$,

$$t_{nucl} \sim AR^{-1} \Delta T_{wall}^{-1/2}, \tag{11}$$

highlighting the importance of the cavity aspect ratio in this case. Furthermore, for small aspect ratios, $AR \ll 1$, and any value of ΔT_{wall}, we can write

$$t_{nucl} \sim \Delta T_{wall}^{-1/2} \exp^{\frac{f}{\Delta T_{wall}}}, \tag{12}$$

which indicates that t_{nucl} becomes essentially independent of AR, while for $AR \gg 1$, the

following relation holds

$$t_{nucl} \sim AR^{-1}\Delta T_{wall}^{-1/2} \exp^{\frac{f}{\Delta T_{wall}}} . \tag{13}$$

Finally, inspection of Equation (9), (12) and (13) reveals that the nucleation time diverges as $\Delta T_{wall}^{-1/2} \exp(f/\Delta T_{wall})$ for small ΔT_{wall}.

The functional dependence of t_{nucl} on AR and ΔT_{wall} represented by the above relations captures the main trends that can be discerned in Figure 4: the weak dependence of the nucleation time on AR for small AR values, its decrease with increasing AR for sufficiently large AR, its rapid decline with ΔT_{wall} for all AR studied, and its sharp increase with decreasing ΔT_{wall}. Also, in order to assess the influence of molecular interactions, variations of the difference between the nucleation times associated with hydrophilic and hydrophobic surfaces, Δt_{nucl}, with ΔT_{wall} are reported in Figure 5, for cavity $AR = 0.5$ and 1. A value greater than zero means that nucleation occurs later on hydrophilic than on hydrophobic surfaces, at the same operating conditions. As shown in Figure 5, wettability effects, amplified by surface nano-structuring, influence the nucleation dynamics for low wall superheats, becoming much weaker with increasing ΔT_{wall}. Specifically, for the parameters used to generate Figure 5, Δt_{nucl} decays significantly for $\Delta T_{wall} > 0.4$, suggesting that the difference in nucleation time between hydrophilic and hydrophobic surfaces is negligible, for both surface geometries investigated. This is consistent with the predictions of Equation (10) which highlights the weak dependence of t_{nucl} on surface wettability at large ΔT_{wall}.

Nucleation occurs earlier on hydrophobic surfaces at low wall superheat because, at these operating conditions, molecular interactions effects prevail over heat transfer phenomena. Molecular interactions are governed by the Lennard-Jones parameters ε_{ij} and σ_{ij}. In particular, the less strong the solid-fluid interaction (more hydrophobic wall) the less energy required to bring a molecule away from the solid surface. Furthermore, for the case of a hydrophobic surface, $\varepsilon_{ff} > \varepsilon_{sf}$ which means that a fluid-fluid interaction will be energetically more favourable than the solid-fluid ones. The presence of a cavity clearly enhances this behavior, as the wall (less favorable interaction) surrounds the fluid in three directions

(bottom, left and right) inside the cavity itself, leading to a sort of fluid entrapment. The only more energetically favorable interaction direction is along the z-axis, out of the cavity. Hence, less energy is required to escape the walls of the cavity leading to a nucleus formation earlier for a hydrophobic wall. As ΔT_{wall} increases the heat transfer starts dominating over molecular interactions and, at intermediate values of ΔT_{wall}, hydrophilic surfaces may lead to slightly faster nucleation events (thanks to a liquid nanolayer which forms on hydrophilic walls). At very high ΔT_{wall}, heat transfer is the only effective parameter which drives the phase transition, explosive boiling is reached and wettability plays no role in determining the nucleation time. This interesting trend is in line with previous works.[30,32,35–38]

Furthermore, this is shown in our mathematical derivation, as can be seen in Equations (10)-(13), where Δt_{nucl} increases with decreasing ΔT_{wall} as variations in wettability are amplified in the exponential terms, $\exp(f/\Delta T_{wall})$ of the nucleation time associated with the hydrophilic and hydrophobic surfaces, and by the fact that $dt_{nucl}/df \sim 1/\Delta T_{wall}^{3/2}$, emphasizing that the nucleation time is very sensitive to surface wettability for small ΔT_{wall}. This effect is particularly pronounced for low cavity aspect ratios and is tempered with increasing AR as shown in Figure 5.

Transition to film-like boiling

Characterizing the transition from nucleate to film-like boiling regimes as a function of AR, ΔT_{wall}, and surface wettability is considered next. We recall here that, at the MD level, gravity is negligible and so is not applied in the simulation setup. As a result, only two regimes can be defined: nucleate boiling and film-like (or, nano-film) boiling, an observation consistent with the literature[23,24,26]. This transition to film-like boiling takes place when the energy provided through the solid wall causes rapid vapour-phase expansion which is not balanced by an adequate supply of liquid in the proximity of the solid-liquid interface.

Figure 6 depicts the effect of surface wettability on nucleate and film-like boiling as a function of the cavity aspect ratio, AR, at $\Delta T_{wall} = 0.2$. Dashed lines correspond to the

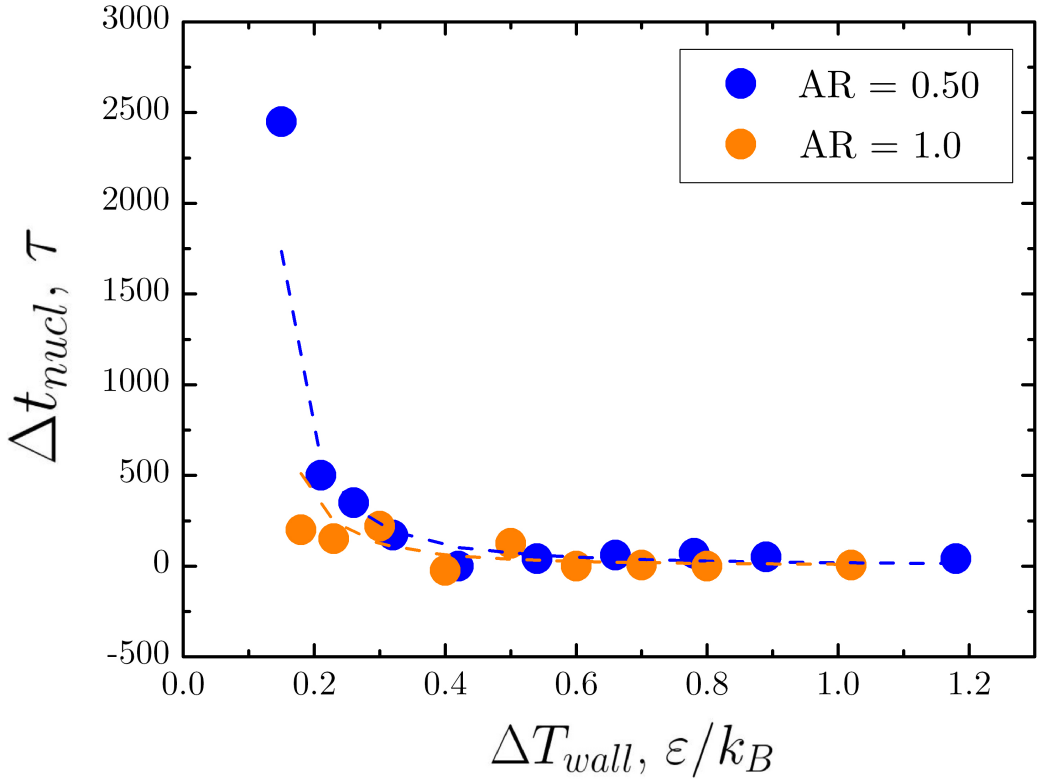

Figure 5: Variation of the difference in nucleation time (measured in reduced LJ units τ) associated with hydrophilic and hydrophobic surfaces, Δt_{nucl}, with the wall superheat ΔT_{wall} for $AR = 0.5$ and $AR = 1$; the wettability parameters are defined in the operating conditions section. The discrete symbols refer to MD simulations results, while the dashed lines correspond to Equation (9) of the CNT-based model.

CNT-based model for nucleate boiling, whereas the dotted lines are drawn to give the reader a clearer understanding of the trends observed for transition to film-like boiling regime. Inspection of Figure 6 reveals that the onset time for nucleate boiling decreases with AR, for the reasons already highlighted above, and that this regime precedes film-like boiling. The time difference between the two regimes increases with AR and, for a fixed AR value, is smallest for the case of the hydrophobic surface. Interestingly, for this surface, the time for transition to film boiling exhibits a weak dependence on AR (see Figure 6, black full circles), which is in contrast with the trends observed for the neutral and hydrophilic surfaces; for these surfaces, the transition time is a generally decreasing function of AR.

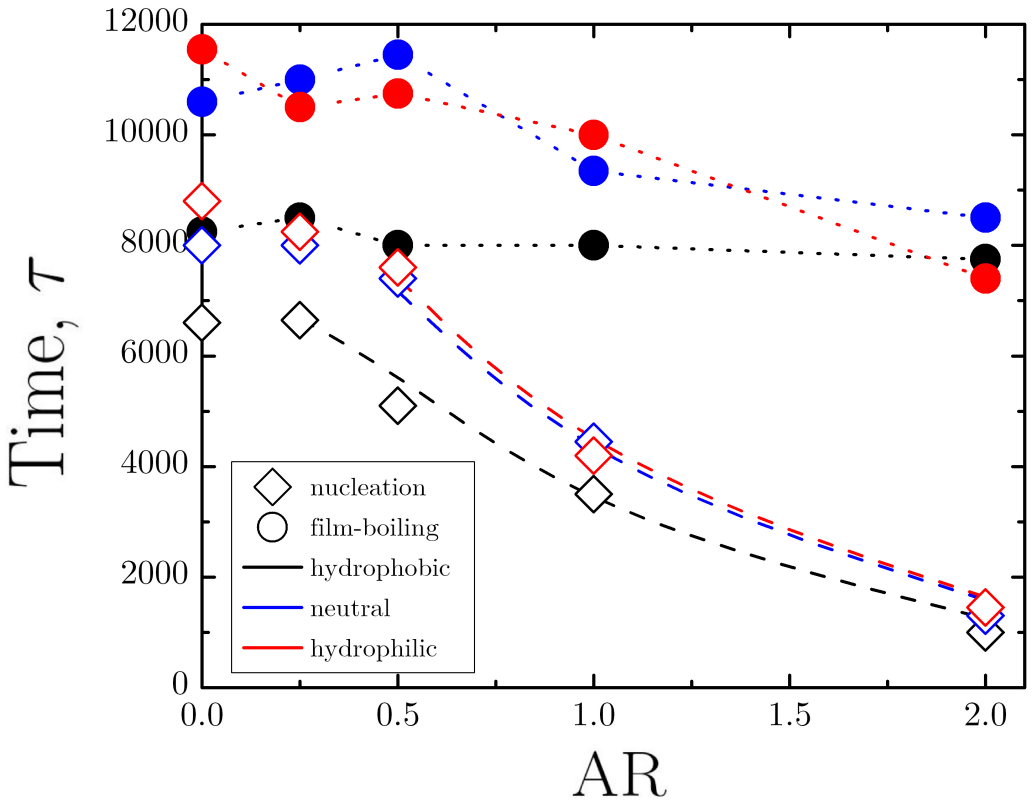

Figure 6: Time (in reduced LJ units τ) to nucleation (diamonds) and to transition to film-like boiling (circles), as function of the cavity aspect ratio, AR, for hydrophobic (black), neutral (blue), and hydrophilic (red) surfaces, characterized by the LJ interaction parameters reported in the operating conditions section, and $\Delta T_{wall} = 0.2$. Dashed lines refer to the nucleation model described by Equation (9), while dotted lines are drawn to show more clearly the trend followed by the transition to film boiling.

This is justified by the fact that for hydrophobic surfaces the liquid-solid interaction (modeled via the LJ potential parameters) is so 'weak' that a very low energy threshold is required to pull a fluid molecule away from the solid wall, leading therefore to a negligible effect of the other parameters (e.g., AR). As a consequence of the weak molecular interactions, the nucleus (or, sometimes, multiple small nuclei) that forms on a strongly hydrophobic surface rapidly expands, leading to the vapor blanket formation. This effect hinders the thermal efficiency of the overall heat transfer process. It is worth noting that no departure frequency can be investigated since gravitational forces are negligible at these

time- and length-scales. A complete picture of the thermal efficiency of the process would require a multi-scale approach beyond the scope of the current work.

Heat transfer analysis

We now examine the evolution of the heat flux and temperature inside the cavity (spatially-averaged across its volume). This is measured over the simulation time in order to quantitatively assess the effect of AR on the heat transfer in pool boiling. Heat flux and temperature profiles shown in this section are further time-averaged every 50τ with the aim of eliminating the noise due to the statistically fluctuating nature of these quantities. Values at each simulation time-step are reported in the SI together with their time-averaged profiles in order to highlight the dependence of the fluctuations from the mean on surface wettability and AR.

In Figure 7 we show the temporal evolution of the rolling time-averaged heat flux inside the cavity for hydrophobic, neutral, and hydrophilic surfaces for $\Delta T_{wall} = 0.2$, with AR varying parameterically. The heat flux is calculated using Equation (4). In line with it, it is normalized by the cavity volume. Hence, different initial values of heat flux are detected at different cavity AR even before nucleation occurs. A standard deviation range is also determined and results in $[0.01, 0.035]$ in LJ units for all the cases investigated. As clearly shown in Figure 7, the heat flux through the cavity decreases with AR and with degree of surface hydrophobicity. This is as expected since nucleation times are shorter (see Figures 4-6), and more vapour is accommodated in the cavity at larger AR and/or higher degree of hydrophobicity, diminishing heat transfer performance due to the the lower thermal conductivity of the vapour in comparison to that of the liquid phase. Furthermore, it is also clear that at sufficiently large cavity aspect ratios, the time-averaged heat flux becomes weakly-dependent on the wettability; the latter is influential at small AR. This is consistent with the trends observed and the explanations provided for the results shown previously in Figures 4-6. The heat flux for smaller cavity AR can be seen from the corresponding probability density functions (PDF) of Figure 7 to have both a larger average heat flux and

much larger fluctuations. These increased fluctuations could result in instantaneous temperature being much larger than predicted from just considering the average, as is common in continuum treatments. This might be expected to result in nucleation at much lower mean temperatures, for example in filament MD fluctuations expedite breakup when included in a continuum models[50]. However, despite this, the smaller cavity AR do not see nucleation more readily than the large AR, suggesting the stabilizing effects of the closer solid walls outweighs this concentration of heat flux, at least at the scale simulated in this work

Rolling time-averaged temperature profiles (averaged every 50τ) in the cavity are shown in Figure 8 for different wetting conditions, with AR varying parameterically, and $\Delta T_{wall} = 0.2$. The discrete points shown in this figure correspond to the times at which nucleation takes place. Figure 8 shows clearly that for a given AR value the cavity temperature increases with surface wettability. The explanation of the dependence of the time-averaged temperature on AR and surface wettability observed here is the same as that proposed above for the heat flux.

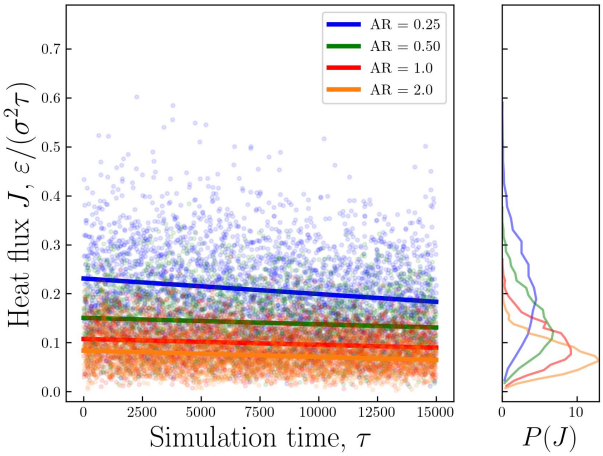

(a) Hydrophobic surface.

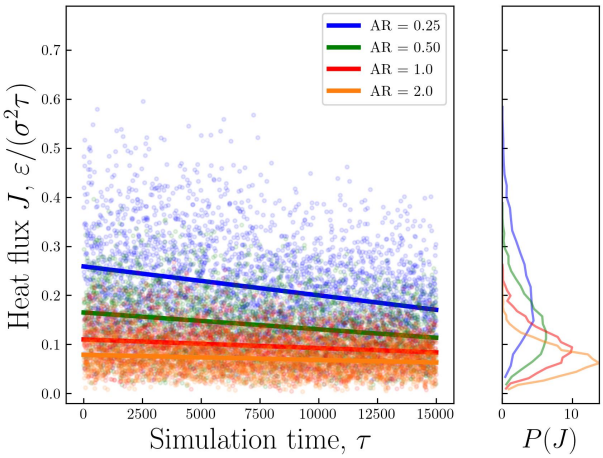

(b) Neutral surface.

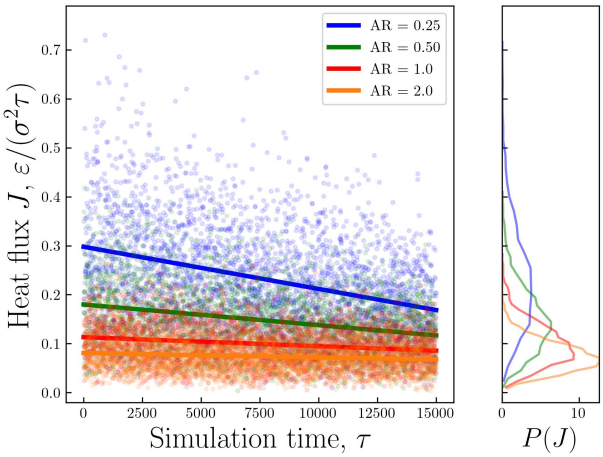

(c) Hydrophilic surface.

Figure 7: Heat flux, J, evolution over simulation time (dots) inside the cavity for different wetting conditions, with AR varying parametrically, and $\Delta T_{wall} = 0.2$. A linear fit of the heat flux fluctuations is reported with a solid line and the corresponding PDF, $P(J)$, on the right side of each graph.

It is instructive to point out that the profiles shown in Figure 8 follow two distinct thermal regimes. For a given surface wettability, an initial stage can be identified around a threshold value of the simulation time approximately equal to 2000τ. The initial stage is accompanied by a rapid increase of the cavity temperature to a local maximum as the liquid is heated by the underlying solid; the temperature profiles associated with all AR values overlap indicating that the dynamics of this stage are not influenced by the cavity. For the smallest AR values studied, and for the hydrophobic surface, the local maximum is followed by a slight dip that then leads a subsequent increase in temperature punctuated by a bubble nucleation event. With increasing surface hydrophilicity, the rapid temperature rise for $AR = 0.25, 0.5$ is followed by a monotonic increase. For larger cavity aspect ratios, the local temperature maximum is followed by a dip, which becomes more pronounced with increasing AR and surface hydrophilicity. This dip precedes a monotonic increase in temperature the rate of which decreases sharply for $AR > 1$. This latter trend is due to the fact that larger cavities are filled with more vapour which provides resistance to heat transfer. This also explains why the mean temperature of the cavities (colored discrete circles in Figure 8) with the largest aspect ratios are lowest for the hydrophobic surface for which the nucleation times are shortest (see Figures 4-6). The discrete points (nucleation events) demonstrate that the onset of nucleation takes place at lower mean temperature in larger cavity AR. In these cases, indeed, the cavity accommodates a wider nucleated embryo which, in turn, can be sustained by lower pressures (and temperatures) according to the Young-Laplace theory[51].

In the perspective of a link with the continuum scale and in the scenario of a more general multiscale framework, we further investigated the heat transfer mechanisms inside the cavity through the analysis of a simple 1D heat transfer model. This approach is very useful to determine the operating conditions where molecular interactions play a key role in linking thermal effects to the continuum scale. The choice of adopting just one spatial dimension in this approach is due to the assumption that temperature gradients are more relevant in the z-direction (that is, the wall-normal direction) than in the x- and y-directions

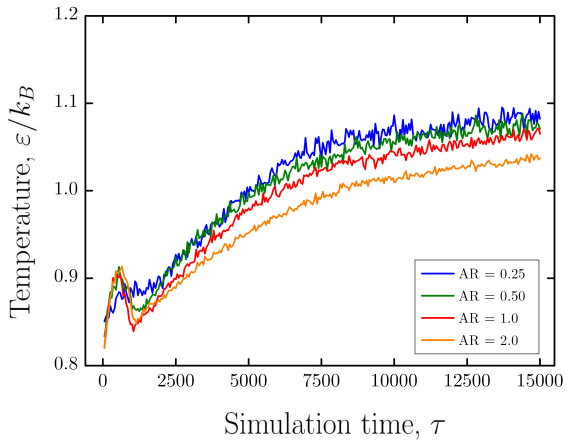

(a) Hydrophobic surface.

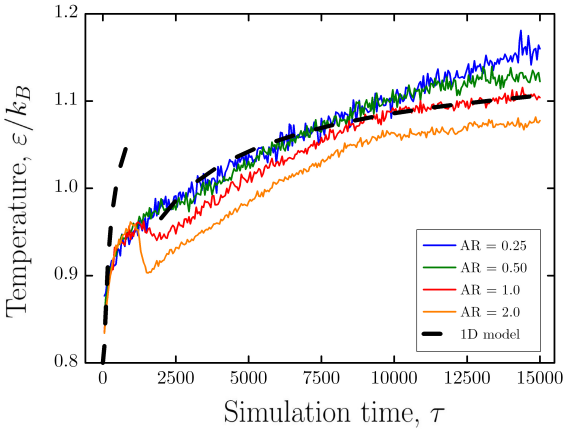

(b) Neutral surface.

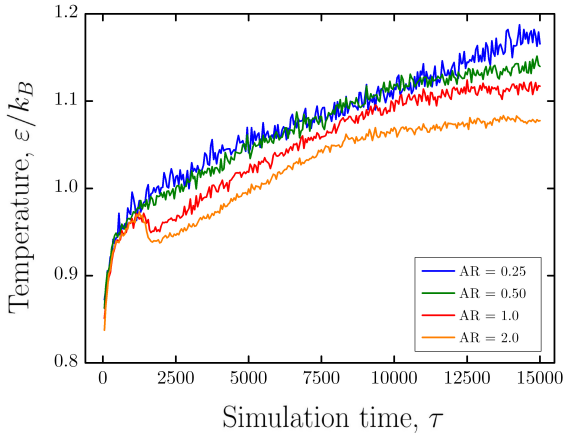

(c) Hydrophilic surface.

Figure 8: Rolling time-averaged (every 50τ) temperature over simulation time (in LJ reduced units) inside the cavity for different wetting conditions, with AR varying parameterically, and $\Delta T_{wall} = 0.2$. The theoretical 1D solution of the heat transfer model is reported in panel (b).

(we recall the presence of periodic boundary conditions in the latter two dimensions, see Figure 1). Furthermore, the MD system showed comparable order of magnitude values for the solid and liquid thermal conductivity at the operating conditions adopted in the current manuscript. We are aware of the error introduced by this assumption but we assume it is acceptable to a first approximation. Accordingly, our simple analysis is based on the use of the heat equation:

$$\frac{1}{\alpha}\frac{\partial T}{\partial t} = \frac{\partial^2 T}{\partial z^2}, \tag{14}$$

where $\alpha = k/(\rho \hat{c}_p)$ represents the thermal diffusivity in which ρ is the fluid density, $\hat{c}_p$ is the fluid heat capacity per unit mass, and k is the fluid thermal conductivity. The boundary and initial conditions read as follows:

$$\begin{aligned} T(z=0,t) &= T_h, \\ T(z=L,t) &= T_0, \\ T(z,t=0) &= T_0, \end{aligned} \tag{15}$$

where $T_0 = 0.8$ is the initial temperature and $T_h = 1.2$ is the heating temperature. Equation (14) admits the following analytical solution which is consistent with Equations (15):

$$T(z,t) = T_h + (T_0 - T_h)\frac{z}{L} + 2\frac{(T_0 - T_h)}{\pi}\sum_{n=1}^{\infty}\left[\frac{e^{-\alpha\mu^2 t}}{n}\sin(\mu z)\right], \tag{16}$$

where $\mu = n\pi/L$. In order to compare the continuum-scale predictions provided by Equation (16) and those from MD simulations, we scale t on τ and set L equal to 180σ. The thermal diffusivity α is also calculated from the MD simulations of pure liquid LJ Argon in the NPT ensemble (the details are in the SI) to be in the range $[0.1, 1]$ in LJ reduced units, depending on the fluid density ρ, at the operating conditions adopted in this work.

We argued above that temperature profiles that show a first peak, local minima, and a smoother profile reaching their plateau correspond to the situation in which a vapour nucleus (embryo) forms inside the cavity. The peak, indeed, corresponds to the sudden liquid-to-

vapour transition. As a consequence of such a phase transition, it is reasonable to assume that the fluid in the cavity will have different values of thermal diffusivity α in the two thermal regimes detected in Figure 8, depending upon the actual value of the density, with a threshold temporal evolution around 2000τ of the simulation time. Hence, we adopted two reasonable values of thermal diffusivity in the time scaling (L^2/α) of the 1D solution reported in Equation (16), assigning to the first regime a liquid-rich α value (i.e., unity in the proper LJ reduced units), and to the second regime (from 2000τ onwards) a vapour-rich α value (i.e., 0.3). By setting the z-coordinate of the centre of the cavity to $z = 20\sigma$, the temperature profile obtained from Equation (16) is shown in Figure 8(b) with the black dashed line. Since no molecular interactions are accounted for in Equation (14), we compare its 1D analytical solution with the neutral surface MD results obtained with the same energetic fluid-solid and fluid-fluid interaction strength characterised by LJ potential parameters $\varepsilon_{sf} = 1$.

Inspection of Figure 8(b) reveals that the dynamics is quite well reproduced in the second regime (for times larger than 2000τ) despite the fact that the explicit presence of a cavity was not taken into account in Equation (14). The agreement between the continuum- and molecular-scale predictions is not as good in the first regime (i.e., up to 2000τ). This leads to the conclusion that the 1D continuum model fails at capturing the correct dynamics of the heat transfer at very short length- and time-scales. This is in line with previous works[52,53] which demonstrated that the Fourier's law-based theory fails at predicting the correct unsteady temperatures distributions at short time- and length-scales for LJ argon systems via MD studies. The time scale at which the largest mismatch between Fourier's law and MD predictions was detected in[52,53] is comparable with ours (order of magnitude of 10^2 ps, following the conversion table reported in supporting information).

From a phenomenological point of view, the discrepancy between the MD and continuum model predictions becomes more pronounced (as shown by our results, Figure 8(b)) when phase transition occurs inside the cavity (first peak of the curves), as reasonably expected by the fact that molecular interactions are the driving factor during the onset of bubble

nucleation and pure heat transfer through a medium (single or two-phase) dominates only after the embryo is formed in the nucleation spot (e.g., cavity).

Phase diagram

The results of the present work are summarized in a phase diagram, shown in Figure 9 for $\Delta T_{wall} = 0.2$. It is worthwhile stressing once more that the choice of investigating the system at low wall superheat is strategic and leads to important conclusions without any loss of generality for a twofold reason: on one side, operating at high wall superheat represents a non-realistic scenario in the context of smart surfaces design for technological applications (e.g., electronic devices subcooling); on the other side, in the interplay of the cavity size, wall wettability and superheat, only at low values of the latter it is possible to appreciate a dominant role of the other two parameters. Indeed, as the wall superheat increases, the peculiar effect of the other two factors fade out. This is confirmed by our analysis presented above on the nucleation model, summarized by Equations (9)-(13). All the investigated points enclosed in a given color border are characterized by the same common property (stated in the corresponding label). A contour plot of the nucleation time is also depicted in the background. Furthermore, the liquid/vapor phase amount inside the cavity is qualitatively reported for each investigated case with a circle: a blue fully-filled circle corresponds to the cavity filled with the liquid phase; white corresponds to the vapor phase. The phase diagram captures the main trends observed in this study; these include the fact that a small cavity AR (e.g. $AR = 0.25$) delays transition to film-like boiling and shows high nucleation times but provides less control on the nucleation site. They also include other phenomena such as the onset of nucleate boiling being promoted by higher cavity AR, which, however, are also associated with the possibility of complete dry-out, undesirable for heat transfer applications. At some operating conditions, eventually, multiple nanobubbles may form and coalesce before growing and expand (light blue region).

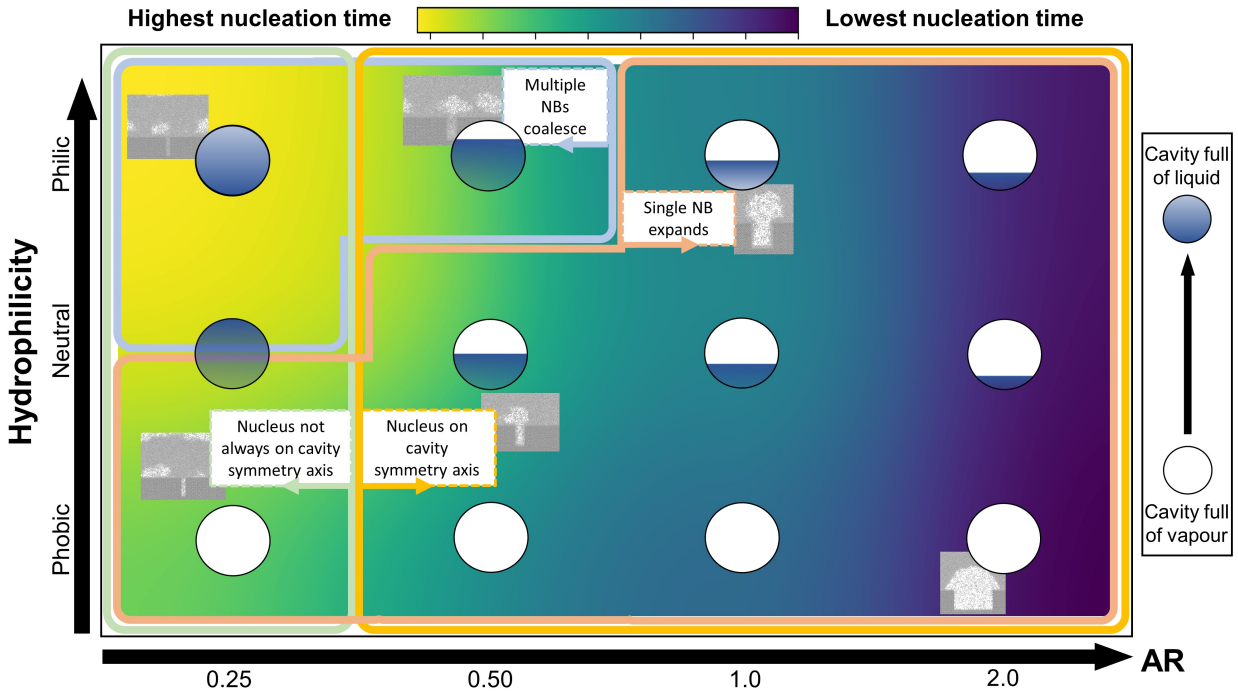

Figure 9: Phase diagram which summarizes the main results and the key mechanisms observed in the MD simulations carried out in this work, at $\Delta T_{wall} = 0.2$. Contour plot of the nucleation time (background) and amount of liquid phase in the cavity (blue/white circles) at each investigated case are also present.

Conclusions

In this work, we studied the effect of surface topography on nucleate pool boiling at the molecular (nano-) scale via non-equilibrium molecular dynamics (NEMD) simulations for a Lennard-Jones (LJ) argon-like system. A molecular tethered wall was employed to create a solid surface with a rectangular cavity, as a heterogeneous nucleation site. We investigated the interplay of several factors via a systematic parametric analysis, with particular focus on the solid wall geometry, in terms of cavity size, wall superheat, and surface wettability. The cavity size was modeled by a dimensionless parameter, the aspect ratio (AR) defined as cavity width-to-depth ratio.

The heat transfer performance of a given surface was evaluated quantitatively in terms of the nucleation time, temperature and heat flux profiles inside the cavity. Additionally, the MD trajectories were qualitatively analyzed. The overall outcome of the parametric analysis can be summarized as follows:

- molecular interactions combined with surface geometry play a crucial role in driving nucleate pool boiling at low wall superheats;
- the cavity size has a twofold effect: on the one hand, it promotes heat transfer to the liquid bulk, and on the other, it drives and controls the onset of nanobubble nucleation;
- heat transfer is more efficient when the cavity predominantly contains liquid: the higher the surface hydrophilicity and the smaller the aspect ratio, the more liquid phase is present in the cavity; in these conditions, however, the control on the nucleation site is poor;
- The higher the cavity aspect ratio and the less hydrophilic the surface, the more the cavity controls the nucleation site (the nucleus forms on the cavity symmetry axis);
- narrow cavities delay transition to film-like boiling, while large cavities promote nucleation (smaller nucleation time);

- large cavity controls the nucleation site (cavity axis), but accelerates the solid surface dry-out which, in turn, is enhanced by the surface hydophobicity.

We also showed that the numerical results of nucleation times at different operating conditions and the interplay of the investigated parameters (cavity size, wettability and wall superheat) can be rationalized by appealing to a classical nucleation theory (CNT)-based model. The thermal behavior at the molecular scale was further compared to that obtained by solving a simple 1D continuum scale model based on the heat equation. This represents a useful strategy to assess and decouple the importance of molecular interactions to the pure heat transfer phenomena, especially with the objective of a future multiscale modelling work. This comparison demonstrated the fact that at very small time- and length-scales, the continuum model fails to predict the dynamic temperature evolution. Finally, the key mechanisms and the fundamentals uncovered by this MD analysis were summarized in a phase diagram which represents the first step of a more general surface topography optimization procedure.

Appendices

Appendix A

Here we provide a comparison between the system size investigated in this work and a similar system but three times larger, in order to evaluate the impact of the system size on the dynamics of bubble formation and growth. Larger simulations (3 times in size, $2.5 \cdot 10^6$ atoms) have been performed and, as a demonstrative study, we report here one case simulated at heating temperature $T_h = 1.5$ and hydrophilic wall in Figure A.1 for cavity $AR = 1$. On the first row there is the system investigated in the current work (10^2 molecular units σ_{ij} scale); a 3-times larger system ($2.5 \cdot 10^6$ particles) is shown on the second row. This

result shows that some similarities can be reached, at least in terms of nucleation time and dynamics of nanobubble formation (yellow line in Figure A.1), despite the dynamics of the nanobubble growth is substantially different.

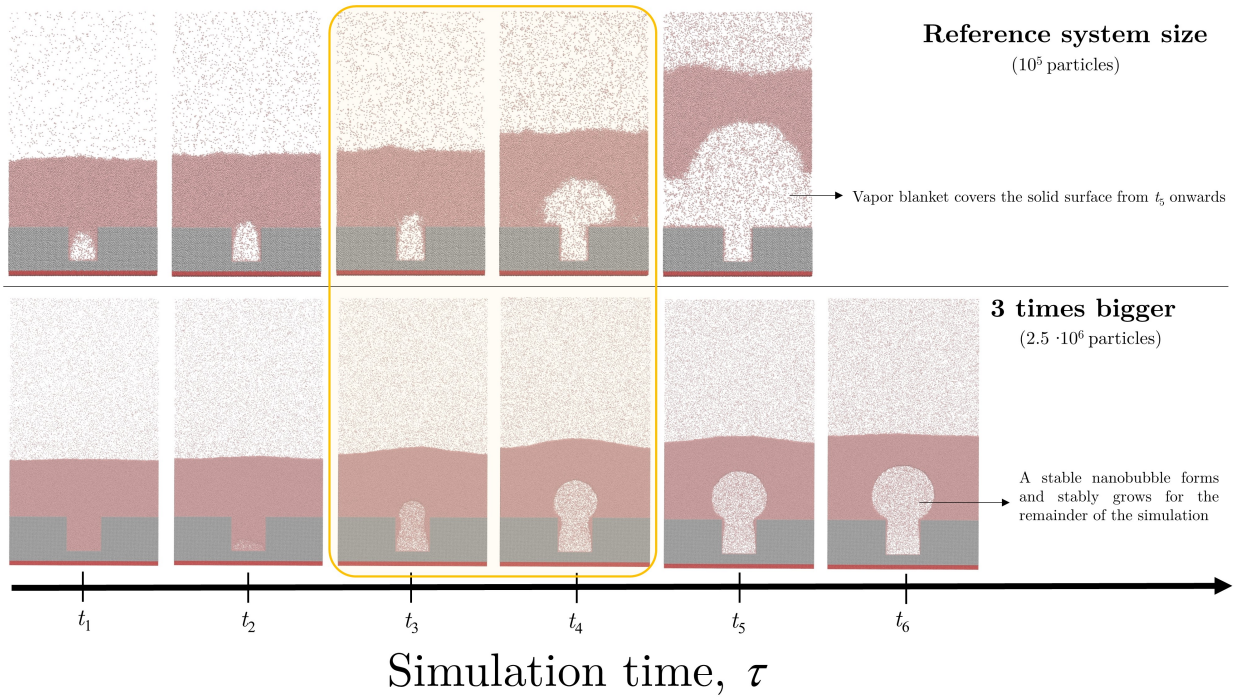

Figure A.1: Temporal evolution of the system over simulation time, in reduced LJ units τ. A comparison between the system size under investigation (first row) and a 3-times bigger system (second row) is shown, for hydrophilic wall at heating temperature $T_h = 1.5$ and cavity $AR = 1$. Similarities about the time for nucleation can be reached (yellow line), despite the growth dynamics is substantially different.

Acknowledgement

This work is funded by the Engineering and Physical Sciences Research Council, UK, funding through project EMBOSS (grant number EP/S019545/1).

Supporting Information Available

The following files are available free of charge.

- Supporting Information: trajectory evolution of the pool boiling over simulation time for all the wettability cases investigated in this work are reported together with further analysis and methodologies applied throughout the manuscript.

References

(1) Bruzzone, A.; Costa, H.; Lonardo, P.; Lucca, D. Advances in engineered surfaces for functional performance. *CIRP Annals* **2008**, *57*, 750 – 769.

(2) Wei, J.; Zhao, J.; Yuan, M.; Xue, Y. Boiling Heat Transfer Enhancement by Using Micro-pin-finned Surface for Electronics Cooling. *Microgravity Sci. Technol.* **2009**, *21*, 159–173.

(3) Karayiannis, T. G.; Mahmoud, M. M. Flow boiling in microchannels: Fundamentals and applications. *Appl. Therm. Eng.* **2017**, *115*, 1372–1397.

(4) Kaushik, S.; Reddy, V. S.; Tyagi, S. Energy and exergy analyses of thermal power plants: A review. *Renewable Sustainable Energy Rev.* **2011**, *15*, 1857 – 1872.

(5) Guan, C.-K.; Klausner, J. F.; Mei, R. A new mechanistic model for pool boiling CHF on horizontal surfaces. *Int. J. Heat Mass Transfer* **2011**, *54*, 3960 – 3969.

(6) Yeoh, G. H.; Zhang, X. Computational fluid dynamics and population balance modelling of nucleate boiling of cryogenic liquids: Theoretical developments. *J. Comput. Multiphase Flows* **2016**, *8*, 178–200.

(7) Zhang, C.; Cheng, P. Mesoscale simulations of boiling curves and boiling hysteresis under constant wall temperature and constant heat flux conditions. *Int. J. Heat Mass Transfer* **2017**, *110*, 319 – 329.

(8) Kim, D. E.; Yu, D. I.; Park, S. C.; Kwak, H. J.; Ahn, H. S. Critical heat flux triggering

mechanism on micro-structured surfaces: Coalesced bubble departure frequency and liquid furnishing capability. *Int. J. Heat Mass Transfer* **2015**, *91*, 1237 – 1247.

(9) Park, Y.; Kim, H.; Kim, J.; Kim, H. Measurement of liquid–vapor phase distribution on nano- and microstructured boiling surfaces. *Int. J. Multiphase Flow* **2016**, *81*, 67 – 76.

(10) Zhang, Y.; Wei, J.; Xue, Y.; Kong, X.; Zhao, J. Bubble dynamics in nucleate pool boiling on micro-pin-finned surfaces in microgravity. *Appl. Therm. Eng.* **2014**, *70*, 172 – 182.

(11) Shojaeian, M.; Koşar, A. Pool boiling and flow boiling on micro- and nanostructured surfaces. *Exp. Therm. Fluid Sci.* **2015**, *63*, 45 – 73.

(12) Wen, R.; Li, Q.; Wang, W.; Latour, B.; Li, C. H.; Li, C.; Lee, Y.-C.; Yang, R. Enhanced bubble nucleation and liquid rewetting for highly efficient boiling heat transfer on two-level hierarchical surfaces with patterned copper nanowire arrays. *Nano Energy* **2017**, *38*, 59 – 65.

(13) Lee, D.; Kim, B. S.; Moon, H.; Lee, N.; Shin, S.; Cho, H. H. Enhanced boiling heat transfer on nanowire-forested surfaces under subcooling conditions. *Int. J. Heat Mass Transfer* **2018**, *120*, 1020 – 1030.

(14) Li, Y.; Duan, C. Bubble-Regulated Silicon Nanowire Synthesis on Micro-Structured Surfaces by Metal-Assisted Chemical Etching. *Langmuir* **2015**, *31*, 12291–12299.

(15) Ryu, S.; Ko, S. Direct numerical simulation of nucleate pool boiling using a two-dimensional lattice Boltzmann method. *Nucl. Eng. Des.* **2012**, *248*, 248 – 262.

(16) Márkus, A.; Házi, G. On pool boiling at microscale level: The effect of a cavity and heat conduction in the heated wall. *Nucl. Eng. Des.* **2012**, *248*, 238 – 247.

(17) Gilman, L.; Baglietto, E. A self-consistent, physics-based boiling heat transfer modeling framework for use in computational fluid dynamics. *Int. J. Multiphase Flow* **2017**, *95*, 35 – 53.

(18) Hoang, N. H.; Song, C.-H.; Chu, I.-C.; Euh, D.-J. A bubble dynamics-based model for wall heat flux partitioning during nucleate flow boiling. *Int. J. Heat Mass Transfer* **2017**, *112*, 454 – 464.

(19) Ilic, M.; Petrovic, M.; Stevanovic, V. Boiling heat transfer modelling: A review and future Prospectus. *Therm. Sci.* **2019**, *23*, 87–107.

(20) Allen, M. P.; Tildesley, D. J. *Computer Simulation of Liquids*, 2nd ed.; Oxford University Press, Inc.: USA, 2017.

(21) Yi, P.; Poulikakos, D.; Walther, J.; Yadigaroglu, G. Molecular dynamics simulation of vaporization of an ultra-thin liquid argon layer on a surface. *Int. J. Heat Mass Transfer* **2002**, *45*, 2087 – 2100.

(22) Wang, Y.-H.; Wang, S.-Y.; Lu, G.; Wang, X.-D. Explosive boiling of nano-liquid argon films on high temperature platinum walls: Effects of surface wettability and film thickness. *Int. J. Therm. Sci.* **2018**, *132*, 610 – 617.

(23) Inaoka, H.; Ito, N. Numerical simulation of pool boiling of a Lennard-Jones liquid. *Phys. A (Amsterdam, Neth.)* **2013**, *392*, 3863 – 3868.

(24) Tang, Y.-Z.; Zhang, X.-G.; Lin, Y.; Xue, J.; He, Y.; Ma, L.-X. Molecular Dynamics Simulation of Nanofilm Boiling on Graphene-Coated Surface. *Adv. Theory Simul.* **2019**, *2*, 1900065.

(25) Yamamoto, T.; Matsumoto, M. Initial Stage of Nucleate Boiling: Molecular Dynamics Investigation. *J. Therm. Sci. Technol.* **2012**, *7*, 334–349.

(26) Diaz, R.; Guo, Z. A molecular dynamics study of phobic/philic nano-patterning on pool boiling heat transfer. *Heat Mass Transfer* **2017**, *53*, 1061–1071.

(27) Diaz, R.; Guo, Z. Molecular dynamics study of contact angle effect on maximum critical heat flux in nano-patterned pool boiling. Proceedings of the 2nd Thermal and Fluid Engineering Conference, TFEC2017 - 4th International Workshop on Heat Transfer, IWHT2017. Las Vegas, NV, USA, 2017; pp 1817–1828.

(28) Yin, X.; Bai, M.; Hu, C.; Lv, J. Molecular Dynamics Simulation of Pool Boiling Heat Transfer of Nanofluids on Rough Walls. ASME 2017 Heat Transfer Summer Conference. Bellevue, Washington, USA, 2017; p V002T10A015.

(29) Yin, X.; Hu, C.; Bai, M.; Lv, J. Molecular dynamics simulation on the effect of nanoparticles on the heat transfer characteristics of pool boiling. *Numer. Heat Transfer, Part B* **2018**, *73*, 94–105.

(30) Novak, B. R.; Maginn, E. J.; McCready, M. J. An Atomistic Simulation Study of the Role of Asperities and Indentations on Heterogeneous Bubble Nucleation. *J. Heat Transfer* **2008**, *130*, 042411.

(31) Chen, Y.; Zhang, C. Role of surface roughness on thermal conductance at liquid–solid interfaces. *Int. J. Heat Mass Transfer* **2014**, *78*, 624 – 629.

(32) Chen, Y.; Li, J.; Yu, B.; Sun, D.; Zou, Y.; Han, D. Nanoscale Study of Bubble Nucleation on a Cavity Substrate Using Molecular Dynamics Simulation. *Langmuir* **2018**, *34*, 14234–14248, PMID: 30398360.

(33) Shahmardi, A.; Tammisola, O.; Chinappi, M.; Brandt, L. Effects of surface nanostructure and wettability on pool boiling: A molecular dynamics study. 2020.

(34) Mukherjee, S.; Datta, S.; Das, A. Molecular Dynamic Study of Boiling Heat Transfer Over Structured Surfaces. *Journal of Heat Transfer* **2017**, *140*, 054503–1 – 054503–5.

(35) Zhou, W.; Li, Y.; Li, M.; Wei, J.; Tao, W. Bubble nucleation over patterned surfaces with different wettabilities: Molecular dynamics investigation. *International Journal of Heat and Mass Transfer* **2019**, *136*, 1–9.

(36) Chen, Y.; Zou, Y.; Yu, B.; Sun, D.; Chen, X. Effects of Surface Wettability on Rapid Boiling and Bubble Nucleation: A Molecular Dynamics Study. *Nanoscale and Microscale Thermophysical Engineering* **2018**, *22*, 198–212.

(37) Hens, A.; Agarwal, R.; Biswas, G. Nanoscale study of boiling and evaporation in a liquid Ar film on a Pt heater using molecular dynamics simulation. *International Journal of Heat and Mass Transfer* **2014**, *71*, 303–312.

(38) Shavik, S.; Hasan, M. N.; Morshed, A. M.; Islam, M. Q. Molecular Dynamics Study of Effect of Different Wetting Conditions on Evaporation and Rapid Boiling of Ultra–thin Argon Layer Over Platinum Surface. *Procedia Engineering* **2015**, *105*, 446–451.

(39) Berendsen, H. J. C. In *Computer Simulation of Biomolecular Systems - Theoretical and Experimental Applications*; van Gunsteren, W. F., Weiner, P. K., Wilkinson, A. J., Eds.; Springer Netherlands: Leiden, 1997; Vol. 2; pp 161–181.

(40) Adamson, A. W.; Gast, A. P. *Physical Chemistry of Surfaces*, 6th ed.; Wiley & Sons: New York, USA, 1997; pp 62–63, 328–335, 465–470.

(41) Shinoda, W.; Shiga, M.; Mikami, M. Rapid estimation of elastic constants by molecular dynamics simulation under constant stress. *Phys. Rev. B* **2004**, *69*, 134103.

(42) Schneider, T.; Stoll, E. Molecular-dynamics study of a three-dimensional one-component model for distortive phase transitions. *Phys. Rev. B* **1978**, *17*, 1302–1322.

(43) Surblys, D.; Matsubara, H.; Kikugawa, G.; Ohara, T. Application of atomic stress to compute heat flux via molecular dynamics for systems with many-body interactions. *Phys. Rev. E* **2019**, *99*, 051301.

(44) Plimpton, S. Fast Parallel Algorithms for Short-Range Molecular Dynamics. *J. Comput. Phys.* **1995**, *117*, 1 – 19.

(45) Humphrey, W.; Dalke, A.; Schulten, K. VMD: Visual molecular dynamics. *J. Mol. Graphics* **1996**, *14*, 33 – 38.

(46) Wen, R.; Ma, X.; Lee, Y.-C.; Yang, R. Liquid-Vapor Phase-Change Heat Transfer on Functionalized Nanowired Surfaces and Beyond. *Joule* **2018**, *2*, 2307 – 2347.

(47) Clouet, E. Modeling of Nucleation Processes. *ASM Handbook, volume 22A Fundamentals of Modeling for Metals Processing, D.U. Furrer and S.L. Semiatin (Ed.) (2009) 203-219* **2009**,

(48) Baidakov, V. G.; Bobrov, K. S. Spontaneous cavitation in a Lennard-Jones liquid at negative pressures. *J. Chem. Phys.* **2014**, *140*, 184506.

(49) Prado, S. C. C.; Rino, J. P.; Zanotto, E. D. Successful test of the classical nucleation theory by molecular dynamic simulations of BaS. *Computational Materials Science* **2019**, *161*, 99 – 106.

(50) Zhao, C.; Lockerby, D. A.; Sprittles, J. E. Dynamics of liquid nanothreads: Fluctuation-driven instability and rupture. *Phys. Rev. Fluids* **2020**, *5*, 044201.

(51) Carey, V. P. *Liquid-Vapor Phase-Change Phenomena: An Introduction to the Thermophysics of Vaporization and Condensation Processes In Heat Transfer Equipment*, 2nd ed.; Taylor and Francis: New York, USA, 2008; pp 138–141.

(52) Liu, Q.; Jiang, P.; Xiang, H. Molecular dynamics simulations of non-Fourier heat conduction. *Prog. Nat. Sci.* **2008**, *18*, 999 – 1007.

(53) Singh, A.; Tadmor, E. B. Thermal parameter identification for non-Fourier heat transfer from molecular dynamics. *J. Comput. Phys.* **2015**, *299*, 667 – 686.

Graphical TOC Entry